

# We are IntechOpen, the world's leading publisher of Open Access books Built by scientists, for scientists

6,900

Open access books available

185,000

International authors and editors

200M

Downloads

Our authors are among the

154

Countries delivered to

TOP 1%

most cited scientists

12.2%

Contributors from top 500 universities



WEB OF SCIENCE™

Selection of our books indexed in the Book Citation Index  
in Web of Science™ Core Collection (BKCI)

Interested in publishing with us?  
Contact [book.department@intechopen.com](mailto:book.department@intechopen.com)

Numbers displayed above are based on latest data collected.  
For more information visit [www.intechopen.com](http://www.intechopen.com)



---

# Single and Coupled Nanobeam Cavities

---

Aliaksandra M. Ivinskaya, Andrei V. Lavrinenko,  
Dzmitry M. Shyroki and Andrey A. Sukhorukov

Additional information is available at the end of the chapter

---

## 1. Introduction

In the coming decade in physics great effort will probably be devoted, among other things, to improving quantum storage and the development of quantum computer. To make use of quantum processes one should avoid decoherence influence of surroundings, or use specifically designed environment to modify the process considered. This is the case when an atom or a quantum dot — nanosized emitter in an active material — is located inside a medium exhibiting modified density of electromagnetic states, e.g., a photonic crystal. In fact, prospects to modify the density of states gave the major motivation to investigate photonic crystals back in the years of their inception. Still they generate large interest from the fundamental cavity quantum electrodynamics perspectives [1–3]. Photonic crystals based structures — beam splitters, cavities, slow light and logic devices — allow for a lot of diverse operations with light. Main advantages of dielectric photonic crystal components over, for instance, their plasmonic analogues are low-loss operation and low-cost production.

Photonic crystals (PhC's) are currently considered as a perspective platform to host low mode volume cavities with high quality factors. A defect can be formed in the photonic crystal lattice by breaking a perfect symmetry of the structure either by removing or shifting basic constitutive units or by local modification of the refractive index. For a quantum dot placed inside a defect in a photonic crystal, the radiation rate is directly connected with the ratio  $Q/V$ , where  $Q$  is the quality factor of the microresonator and  $V$  is the mode volume.

Basically, for a photonic crystal featuring a full three-dimensional (3D) band gap, a defect in it should give the highest possible  $Q$ -factor. However, fabrication of photonic crystals with full 3D band gaps, e.g., inverted opals or woodpile structures and defects in them is quite complicated. That is why a standard way to create a cavity is to use a 2D photonic crystal platform, mostly silicon or GaAs slabs with perforation. Position of holes in such slab is manually defined, giving thus flexibility in the design and optimization of cavities and other

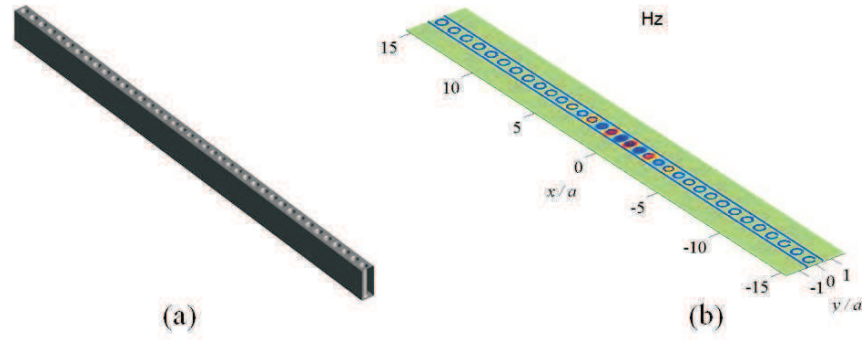


**Figure 1.** (a) The geometry of nanobeam cavity. (b) Magnetic field in resonance.

photonic components. A variety of high- $Q$ , low- $V$  cavity designs were proposed based on structural modifications in photonic crystal matrices [4–9].

The main channel for losing energy from a free-standing membrane cavity is through the coupling to radiative leaky modes. In the plane of the slab the 2D photonic crystal acts as a distributed Bragg mirror, thus in-plane ( $\parallel$ ) leakage of radiation from the photonic crystal cavity is typically small. In the out-of-plane ( $\perp$ ) direction light is primarily confined by total internal reflection, thus the magnitude of  $\mathbf{k}_{\perp}$  vector should be as small as possible to reduce losses. There exists connection between in-plane and out-of-plane wave vector components stipulated by coupling to radiation modes. Increase in  $\mathbf{k}_{\perp}$  originate from  $\mathbf{k}_{\parallel}$ -vectors lying close to the light cone and the usual approach employed for optimization of cavities is through some guess for the design that would give  $\mathbf{k}_{\parallel}$  lying far enough from the light cone. Also in-plane mirror imperfections can lead to parasitic coupling to vacuum modes for some structures.

If some design is to be optimized to achieve high  $Q$  – mode, this should be done gently without abrupt changes in the structure geometry or refractive index, because otherwise undesirable leakage of radiation can appear. In this sense the best designs for optimization are waveguide-like ones [10] and nanobeam cavities [11, 12], Fig. 1, having simple arrangement of field maxima and minima along the straight line. Such 1D arrangement allows for application of the mode-matching rule [13], when the hole sizes and PhC pattern change gradually going from the cavity center towards the mirror part [14, 15]. For modes with more complicated symmetries, for instance, a hexapole mode in a one-hole-missing membrane [16], this approach is not readily applicable since the mode by itself can easily vanish due to a moderate geometry modification.

A photonic crystal nanobeam cavity created by perforating a photonic wire waveguide (nanoridge waveguide) with a row of holes, Fig. 1, reaches a  $Q$ -factor comparable to that of a photonic crystal membrane resonator while being much more compact and easy in fabrication. Even for a nanobeam cavity in a low refractive index material like  $\text{SiO}_2$ , fairly high  $Q$ -factors of several thousands were measured experimentally [17]. Besides a high  $Q$ -factor, a nanobeam cavity exhibits a set of other desirable characteristics: low mode volume  $V$  (less than the cubic wavelength of light) and the smallest footprint size among other high- $Q$  cavities. This stimulates intensive investigations of nanobeam-related acousto-optic and optomechanic interactions [18, 19]. Recently all-optical logical switching [20] and quantum dot laser [11] have been demonstrated in nanobeam cavities. Tiny size of nanobeam cavities makes them also very promising for densely integrated photonic circuits.

Of particular interest are ensembles of cavities [21] with quantum dots placed inside. Full three-dimensional description of such systems is not yet a routine task, but it is very important for fundamental investigations of light-matter interactions [22–24]. Side-coupled nanobeams [14, 25, 26] offer new possibilities for shaping optical fields at nanoscale, which is potentially beneficial for various applications including trapping and manipulation of particles [27], sensing and optical switching through optomechanical interactions with suspended nanobeams [18, 19].

Strong and controllable coupling [28] is also required to create low-threshold lasers [29], observe Fano line shapes [30], design field concentrators for detection of molecules [26], create flat slow light passbands [31, 32], holographic storage [33], and enhance nonlinearities [34]. Formally, consideration of coupled cavities can be made in direct analogue with the molecular mode hybridization, that is why coupled resonators are often called ‘photonic molecules’ [35, 36].

On the other hand, for some applications reduction of coupling strength between the resonators is the key. Indeed, interaction between optical components can shift operation wavelength of the device. Avoiding of parasitic coupling of components is crucial for photonic integrated circuits and in optic network design. Realization of flexible control over the modes in arrays of nanocavities by their rearrangement contributes to the development of on-chip quantum-optical interferometers [23] and quantum computers [24].

## 2. The finite-difference frequency-domain method

Optics and photonics are rapidly developing fields building their success largely on use of more and more elaborated artificially nanostructured materials. To further advance our understanding of light-matter interactions in these complicated artificial media, numerical modeling is often indispensable.

One of the most challenging computational tasks is evaluation of the  $Q$ -factor of a resonator. The traditional way here is to use the finite-difference frequency-domain (FDTD) method to simulate these spatially extended structures with the subsequent extraction of  $Q$  by analyzing the ring-down of electromagnetic field components. Such time-domain simulations can take considerable time up to several days per single run for a high- $Q$  3D resonator.

If several modes are traced in the time domain within a single run, the accuracy of the  $Q$ -factor determination may degrade. The extraction of the separate mode field profiles requires the Fourier transformation of field evolution stored for some space volume and time interval. If two modes are degenerate, separating them with the FDTD method is even less trivial, especially if at the degeneracy point the coupled structure does not have a plane of symmetry allowing to split the modes by the appropriate domain reduction.

On the contrary, the frequency domain techniques grant an opportunity to get straightforwardly in one run maps of several modes, their eigenvalues and quality factors. When modes in the coupled cavities are degenerate, we can get an idea how they may look like — though the picture becomes now ambiguous.

As an competitive alternative to the time domain modeling we employ here the 3D finite-difference frequency-domain (FDFD) method. Details of the method are published

elsewhere [37]. The eigenmode equation in the FDFD method is obtained through combining Maxwell's equations into the second-order differential equation for  $\tilde{\mathbf{H}} \equiv \sqrt{\mu} \mathbf{H}$ :

$$\sqrt{\mu^{-1}} \nabla \times \epsilon^{-1} \nabla \times \sqrt{\mu^{-1}} \tilde{\mathbf{H}} = \omega^2 \tilde{\mathbf{H}}. \quad (1)$$

Then,  $Q$ -factor is straightforwardly found as  $Q = \text{Re}(\omega)/2\text{Im}(\omega)$  after solution of the eigenproblem for complex  $\omega$ . No other elaborated post-processing is needed. Thus transition to the frequency domain for cavity eigenmode analysis is very natural as it greatly reduces the computation time.

To impose boundary conditions we use perfectly matched layers (PMLs). The PMLs were originally designed to absorb propagating electromagnetic waves while evanescent fields can be even intensified in them. High- $Q$  cavities have extremely intensive fields around them. To keep the domain size reasonably small and at the same moment to avoid evanescent waves to fall into the PMLs we use the free space squeezing procedure to set a buffer layer. For all simulations in this chapter we use one-lattice-constant-thick buffer layers. Two squeezing functions are applied to project infinite open space to this buffer layer: inverse hyperbolic tangent ( $\text{arctanh}$ ) function and steeper  $x/(1-x)$  function. To make our simulations efficient we also use the solution-adapted continuous grid density variation of lower resolution in the extended photonic crystal mirror part. If a smooth analytic function is used to create a non-equidistant mesh, it assures the impedance matched transformation leading to the absence of reflection in the transition region to the finer mesh. The symmetries of resonators are exploited to reduce the computational domain. For further insight in the FDFD simulations and free space squeezing we refer to [37].

### 3. Single nanobeam

#### 3.1. Modeling in 2D: High- $Q$ design

At the beginning we tailor the nanobeam cavity design in 2D to get a high- $Q$  TE-mode (electric field in the  $x-y$  plane). Fig. 2 shows a basic nanobeam sketch used to consider various cavity designs: a nanowire of refractive index 3.4 is suspended in air and has 20 holes in its half. Perforation consists of two regions: the chirped mode matched defect region and long periodic part acting as a Bragg reflector. In the reflecting part the lattice constant is  $a$ , hole diameter is  $d$  and total width of a nanobeam  $t = 1.0a$ . In the defect region the modified hole diameters and lattice constants are  $d_n$  and  $a_n$ , respectively, where  $n$  numbers a segment in the defect part of the cavity. For 2D simulations we put  $\Delta x = \Delta y$ . Along  $y$ -direction  $1a$ -wide buffer layers are squeezed with the hyperbolic arctangent function covered by PMLs on 1/3. No air buffer is used along  $x$ -direction, just PMLs comprising 3 grid cells.

Intuitive variation of the defect region parameters – holes radii  $d_n$  and lattice constant  $a_n$  – in order to maximize the  $Q$ -factor led us to the following conclusions. First of all, when both parameters are constant ( $a_n=\text{const}$ ,  $d_n=\text{const}$ ) but differ from those in the reflecting part, the  $Q$ -factor can approach  $10^5$ . Second, if one of the parameters slowly decreases in the defect region towards the center (for example,  $a_n=\text{const}$  and  $d_n$  is varied, or vice versa),  $Q$  rises to  $10^6 \div 10^7$ . Third, only if both  $a_n$  and  $b_n$  are gradually decreased from the periphery to the center of the cavity,  $Q$  reaches the highest value around  $10^8 \div 10^9$  in 2D. In 3D it is usually one to two orders of magnitude less.

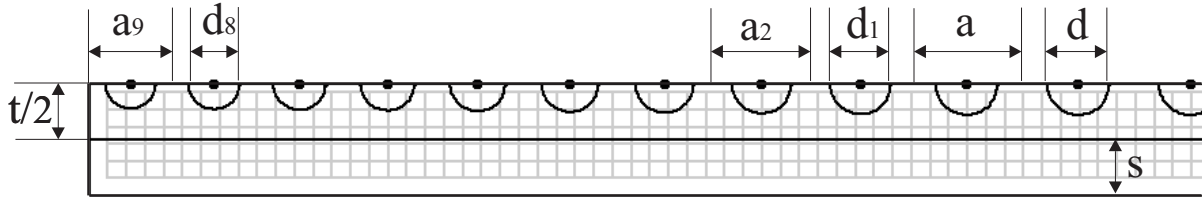


**Figure 2.** Nanobeam quarter,  $x$ -direction is pointing along the nanobeam perforation,  $y$ -direction is along the nanobeam width,  $s$  shows the buffer around the nanobeam.

	Design 1	Design 2	Design 3
Mirror: hole diameters	$d = 0.54a$	$d = 0.6a$	$d = 0.55a$
Defect: number of holes	$n = 1 \dots 9$	$n = 1 \dots 9$	$n = 1 \dots 9$
Defect: hole diameter	$d_n = \frac{d}{\sqrt[10]{n}}$	$d_n = 0.6a_n$	$d_n = d - 0.012na$
Defect: lattice constant	$a_n = \frac{d_n}{0.6}$ $a_1 = 0.8a$	$r_1 = \frac{1}{0.843a}, r_2 = \frac{1}{a}$ $a_n = \frac{1}{r_1 + \frac{r_2 - r_1}{9}n}$	$a_n = \frac{d_n}{0.6}$

**Table 1.** Different designs of the nanobeam cavity sketched in Fig. 2.

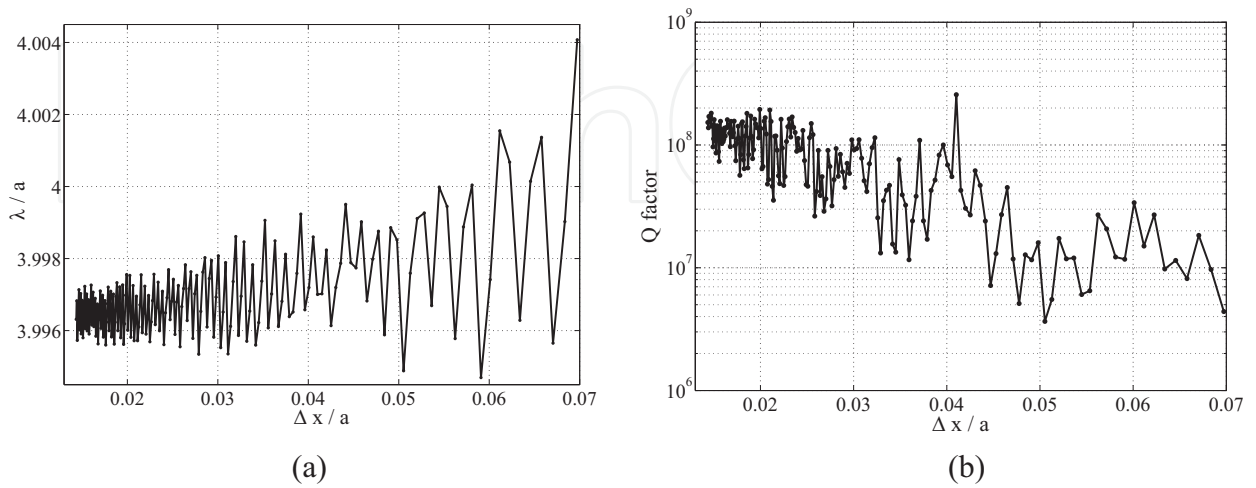


**Figure 3.** 2D (a)  $Q$  and (b)  $\lambda$  convergence for the third design from Table 1.  $\Delta x = \Delta y$ ,  $y$ -buffer is  $1a$ -wide ( $\arctanh$  squeezed) with  $1/3$  covered by the  $y$ -PMLs,  $x$ -PMLs comprise 3 grid cells.



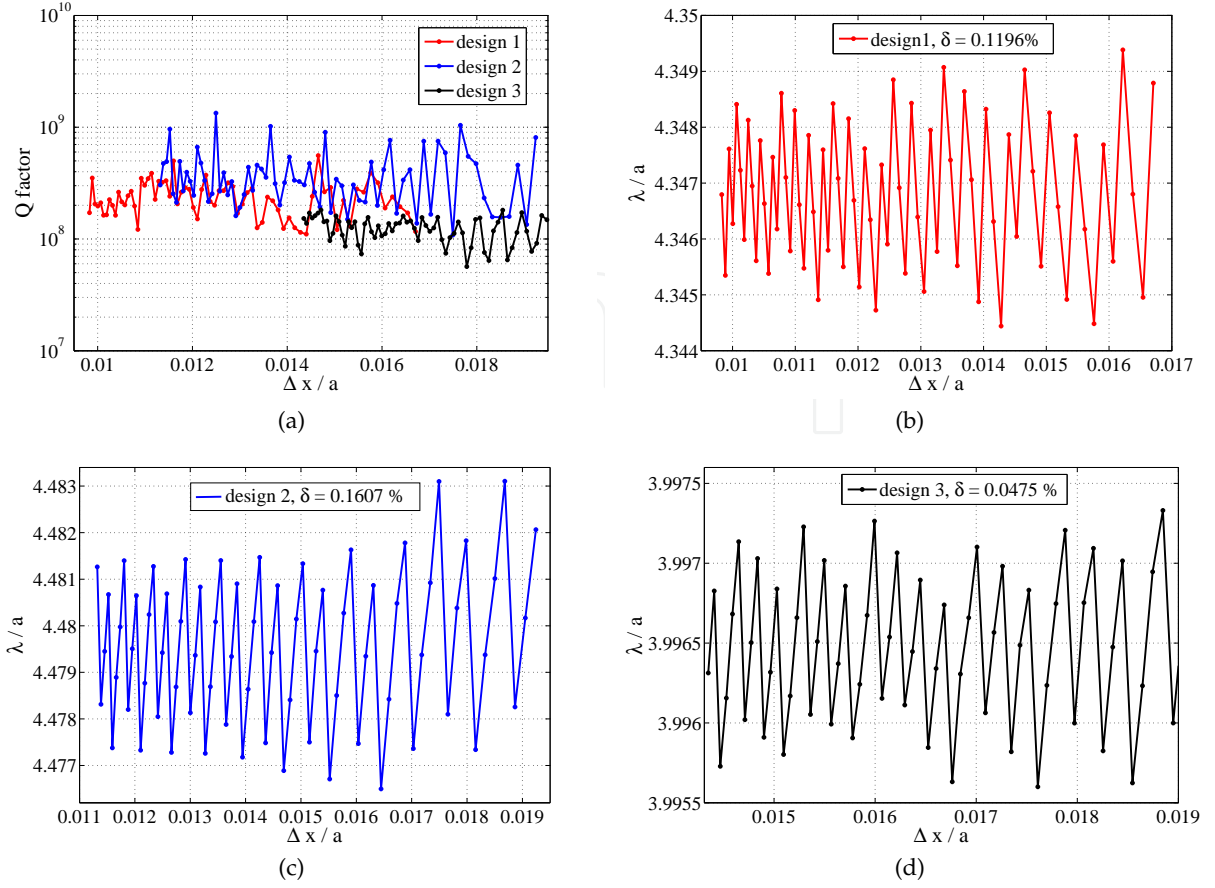


**Figure 4.** (a) Q-factor and (b)-(d)  $\lambda$  convergence for the three designs in the region of fine resolutions with estimation of spread  $\delta$  shown in the legend. 2D simulations with  $\Delta x = \Delta y$ ,  $1a$ -wide buffer layers (*arctanh* squeezed) along the  $y$ -direction are covered on  $1/3$  by  $y$ -PMLs,  $x$ -PMLs – 3 grid cells.

Having established that  $a_n$  and  $d_n$  should vary we investigated ways to do that. Several laws to tailor the nanobeam design have been compared. Among them are  $1/\sqrt[10]{n}$  multiplier to decrease both  $a_n$  and  $d_n$  (design 1); cavity formation similar to [12] when the hole diameter and lattice constant vary linearly in the reciprocal space (design 2); and linear decrement of  $a_n$  and  $d_n$  towards the middle of the nanobeam (design 3) [15]. With all mentioned designs we were able to rise the Q-factor to the order of  $10^8$  simply by playing with parameters. Table 1 summarize details of different nanobeam cavity designs. For the first and third designs we start by defining modified hole diameter  $d_n$ , and modified segment size  $a_n$  is calculated afterwards. For the design 2 calculation of modified lattice constant  $a_n$  precedes evaluation of the defect hole diameters.

In Fig. 3 an example of the  $Q$  and  $\lambda$  convergence curves for the design three is plotted starting from a quite coarse resolution, while Fig. 4a–d allows to do more detailed comparison between different designs in the region of fine resolutions. All of the designs from Table 1 have similar Q-factor values, Fig. 4a, the design three revealing faster convergence than others. In Fig. 4b–d the eigenwavelength convergence is plotted for the three designs in the same  $\Delta x$  range as in Fig. 4a. To estimate the convergence rate, relative spread  $\Delta\lambda$  of convergence curves around a central wavelength  $\lambda_0$  can be introduced:  $\delta = \frac{\Delta\lambda}{\lambda_0} 100\%$ . The design three has  $\delta$  one order less than the designs one and two even at rougher resolutions.

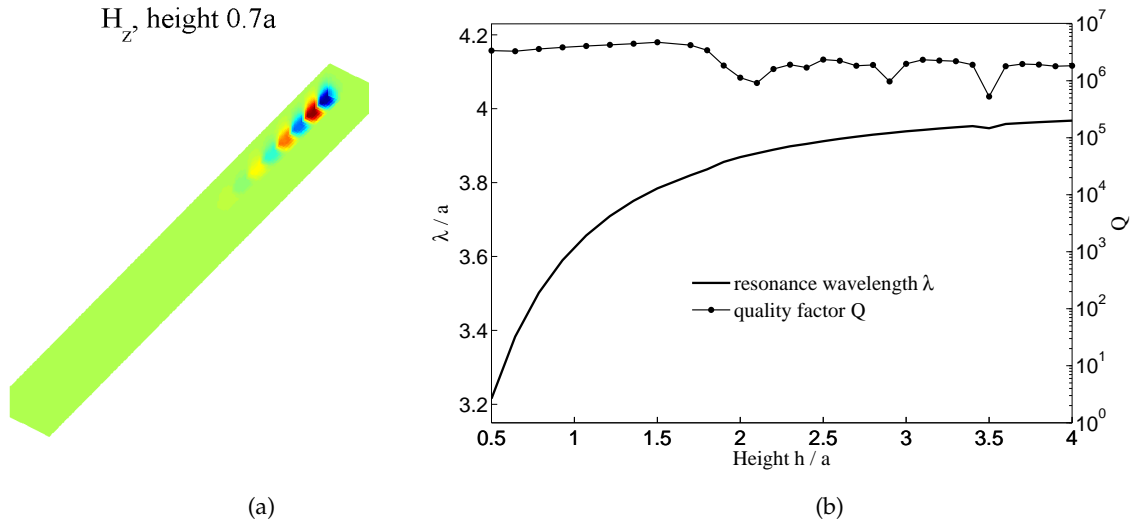


**Figure 5.** (a) Field patterns of the TE mode in the nanobeam cavity of the height  $0.7a$ . Only the quarter of the nanobeam is shown. (b) Resonance wavelength  $\lambda$  and  $Q$ -factor dependence on the nanobeam height  $h$ . 3D simulation is made with cubic grid cell of  $0.07a - 0.1a$  size,  $1a$ -buffer along both  $y$  and  $z$ -directions is *arctanh*-squeezed,  $a/3$  distance goes for PMLs,  $x$ -PMLs are 3 cells wide.

Thus, we ended with the sizes modification according to a linear law as better converging numerically. Design 3 is used in all further nanobeam cavity simulations. We think that the better numerical stability can lead also to the better stability with respect to the fabrication imperfections.

We pay special attention to this analysis, because the  $Q$ -convergence curve for the nanobeam cavity is worst than that for the PhC membrane resonator, compare with the results in [37]. A one-dimensional PhC basis for the nanobeam cavity is somewhat less reflecting than a 2D stop band utilized in the membrane resonators. Thus, if a small imperfection in a 1D mirror is present (due to either some perturbations during fabrication or inaccuracy due to finite difference description), radiation can easily escape through sidewalls of the 1D mirror, while in the case of a membrane leaking radiation can be captured in all in-plane directions in the surrounding 2D-PhC mirror. As discussed in Introduction, undesirable coupling to vacuum modes is directly connected to  $k_x$  (in 1D  $k_{||} = k_x$ ) distribution around the light cone, and thus even a tiny variation in  $k_x$  might lead to the strong variation in the  $Q$ -factor, while the total wave vector is changed only slightly by perturbations and  $\lambda$ -curve preserves good convergence.

### 3.2. Modeling in 3D

In the 3D modeling a defect region in the nanobeam cavity is perforated according to design 3 (see Table 1). In 3D again  $1a$ -wide buffer layers along  $y$  and  $z$ -direction are covered by PMLs on  $1/3$ . No air buffer is used along  $x$ -direction, just PMLs comprising 3 grid cells. We use either equidistant or non-equidistant meshes, but always set  $\Delta x = \Delta y = \Delta z$  in the center of the nanobeam (the defect region). Then for non-equidistant meshes  $\Delta x$  can be stretched up to three times towards the periphery of the nanobeam.

Fig. 5 shows dropping of the resonance wavelength of the TE-mode in the nanobeam cavity with the reduction of its height  $h$  along the  $z$ -direction. Decreasing of the nanobeam height



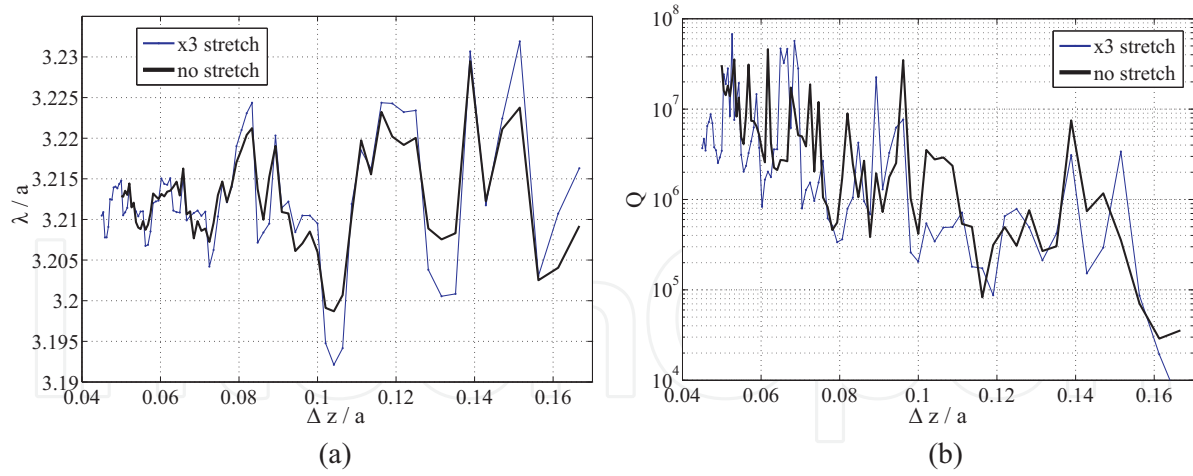


**Figure 6.** (a) The resonance wavelength and (b)  $Q$ -factor versus grid step for uniform ( $\Delta x = \Delta y = \Delta z$ ) and nonuniform  $x$ -mesh with three times stretching in the mirror part ( $\Delta x = \Delta y = \Delta z$  in the center of the nanobeam). Buffer size along the  $y$  and  $z$  directions is  $1a$  ( $x/(1-x)$  squeezed) with  $1/3$  occupied by the PMLs, the PMLs width in the  $x$ -direction being 3 grid cells.

also greatly minimizes the mode volume, for example, for height  $h = 0.5a$  it is equal to  $0.86 (\lambda/n)^3$ . We keep this nanobeam height for the modeling of the coupled cavity structures.

Figure 6 demonstrates the  $Q$ - and  $\lambda$ -convergence for this height. The  $\lambda$  calculation has uncertainty less than 1% at sufficient resolutions while the convergence of  $Q$  is more unstable than in 2D. We can remind here that low accuracy of the  $Q$ -factor evaluation reflects high sensitivity of the  $Q$ -factors of 1D PhC-based structures to imperfections in their finite-difference description. And in 3D model we have an additional channel ( $z$ -direction) for coupling of a genuine cavity mode to leaky modes compared to the 2D case, what causes degradation of convergence. It is interesting to note that instabilities do not show up in Fig. 5. With variation of the height we do not change the resolution along the 1D mirror and thus  $k_x$  distribution is completely the same for all height values.

## 4. Coupled nanobeams

### 4.1. Two coupled nanobeams

When two identical cavities are positioned parallel to each other, their modes undergo hybridization. Supermodes possess symmetric or anti-symmetric profiles [25] and shift in frequency up and down from the former level. We will refer to this splitting as frequency detuning. The frequency detuning between the supermodes normally increases as the cavities are brought closer, and such sensitivity to the separation can lead to pronounced optomechanical phenomena. This may have various applications including the mechanically-induced frequency conversion for optical waves [38]. Analogous effects of modes splitting occur in coupled periodic waveguides, where several channels can enrich the band structure of a single mode waveguide in a controllable way, e.g. in slow light modes positioning at the band edge on demand [39].

#### 4.1.1. Analysis of field profiles in 2D

First, we analyze two side-coupled nanobeam cavities as in Fig. 7a, where the right half of the structure is shown (the left half is symmetric). The individual identical nanobeams have

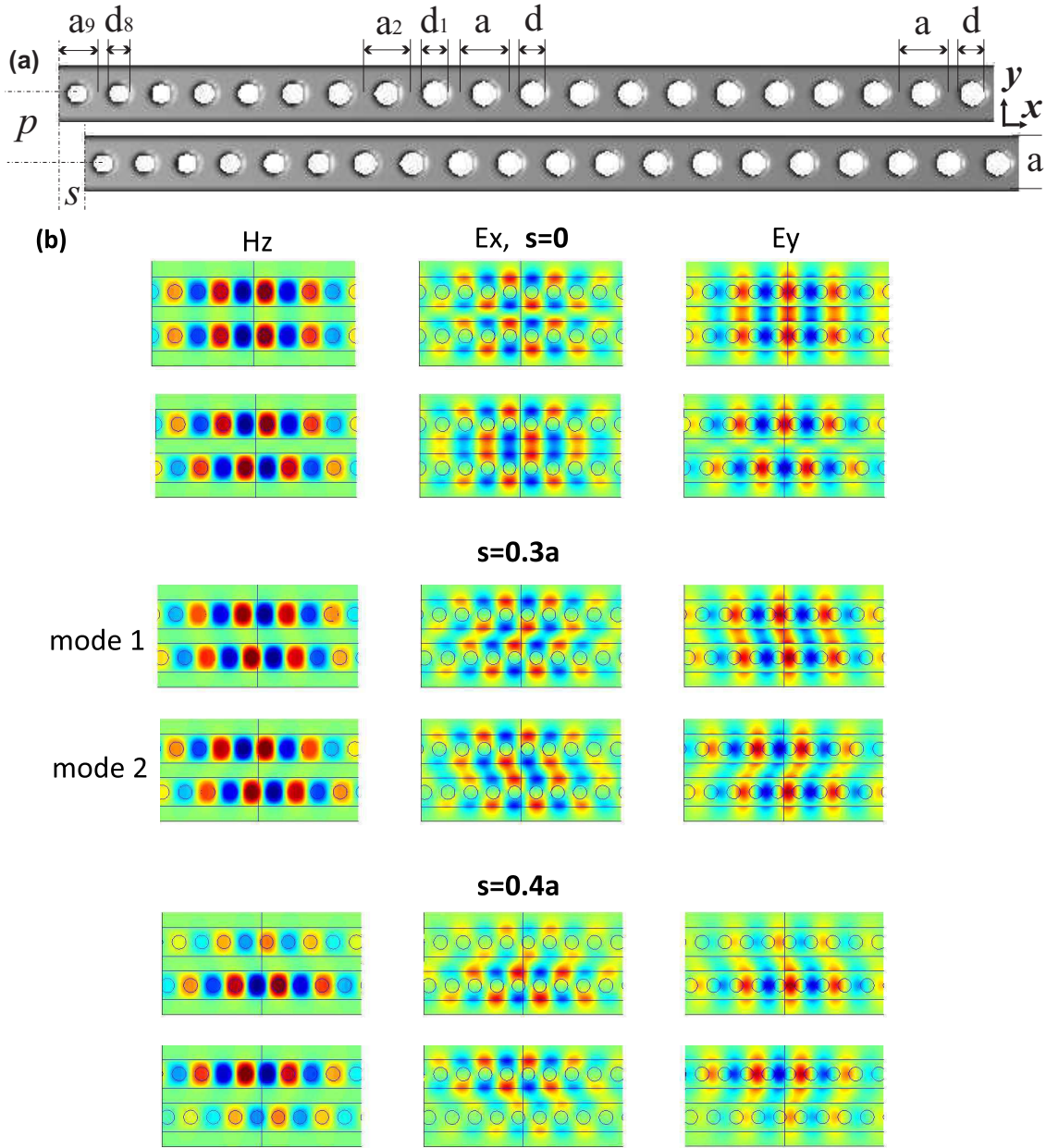


**Figure 7.** (a) Two nanobeams, each of width  $t = a$ , refractive index  $n = 3.4$  and drilled with 20 holes in each half, separated one from another by  $p$  and shifted longitudinally by  $s$ . (b) 2D field profiles for modes (labeled mode 1 and 2) in coupled cavities with zero,  $s = 0.3a$  and  $s = 0.4a$  longitudinal shifts when separation  $p = 1.5a$ , for each shift mode one being positioned at the top while mode two takes the bottom position.

design 3 from Table 1. This gives a linearly chirped array of elements (holes), while other designs are also possible; the general mode properties are usually similar for different chirp functions. The resonance wavelength of a single nanobeam in 2D is  $\lambda = 3.9964a$ ,  $Q = 1.5 \cdot 10^8$ , Fig 3. Two parameters describe the position of the second nanobeam cavity relative to the first one: transverse separation  $p$  and longitudinal shift  $s$ , Fig. 7a.

To make the computational work efficient all modeling is done at the beginning for 2D nanobeam geometries with the main emphasis on the field patterns redistribution as the coupled resonators are rearranged. As we are interested in coupling effects between two nanobeam resonators when they are shifted longitudinally and transversally with respect

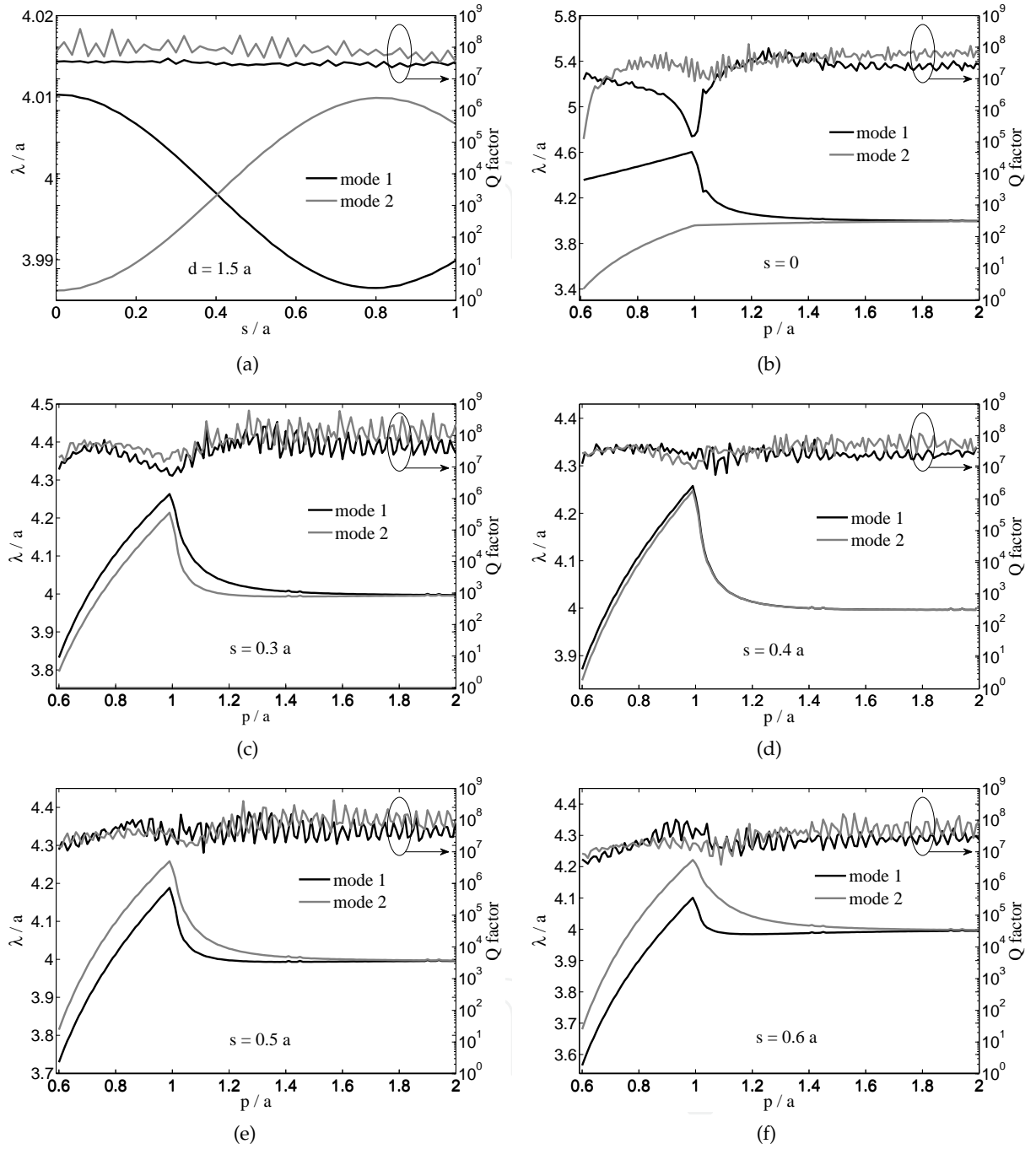


**Figure 8.** (a) Detuning of the mode one and mode two vs the longitudinal shift. Transverse separation between nanobeam axes is  $p = 1.5a$ . (b)-(f) Resonance wavelengths and  $Q$ -factors of eigenmodes in side-coupled nanobeam cavities vs. their transverse separation  $p$ . Results are presented for four different shifts: (b)  $s = 0.0a$ ; (c)  $0.3a$ ; (d)  $0.4a$ ; (e)  $0.5a$ , (f)  $0.6a$  as indicated by labels. Separation of  $1.0a$  and less corresponds to a single dielectric beam with two rows of holes. 2D simulations are made with  $\Delta x = \Delta y \simeq 0.004a$ .  $1a$ -wide  $y$ -buffer is  $\text{arctanh}$  squeezed with half of it covered by PMLs.  $x$ -PMLs comprise 3 grid cells.

to each other, we need to perform a new computational cycle each time the structure is modified by a small displacement. In the 2D case the execution time is several minutes even for the huge resolution such as  $n_{tot} = 6 \cdot 10^5$  grid nodes available with a 8Gb station. For 2D simulations we put  $\Delta x = \Delta y \simeq 0.004a$ . Along  $y$ -direction  $1a$ -wide buffer layers are squeezed with the inverse hyperbolic tangent function and covered by PMLs on  $1/2$ . No air buffer is used along  $x$ -direction, just PMLs comprising 3 grid cells.

Mode profiles in Fig. 7b show formation of the symmetric and antisymmetric cavity modes when two nanobeam resonators are brought together without shifting,  $s = 0$ . Magnetic field hot spots coincide with the location of the holes. With separation  $p = 1.5a$  we see only electric field in the air gap between the nanobeams. When one of the nanobeams is subjected to a longitudinal shift the system loses its symmetry and modes cannot be specified anymore as symmetric and antisymmetric. We will refer to notation ‘mode 1’ and ‘mode 2’ to call transformations of even and odd modes respectively with gradual shift starting from zero.

At zero longitudinal shift  $s = 0$   $E_x$  component of mode 1 and  $E_y$  component of mode 2 have a node plane passing through the middle of the air gap between the nanobeams ( $y = 0$ ). For applications requiring high field intensities it would be preferable to avoid these zero-valued fields. It turns out that as the nanobeams are gradually shifted from  $s = 0$  the node planes for both of these modes components are substituted by a plane with high field intensities, see Fig. 7b for  $s = 0.3a$ . At the same moment other electric field components ( $E_y$  for mode 1 and  $E_x$  for mode 2) still preserve quite high field values. Thus, a small longitudinal shift helps in removing areas of zero fields in the air gap and makes the electric field intensity more uniform across the gap between the two nanobeams. The field uniformity in the shifted nanobeams can be further improved by moving the nanobeams closer in the transverse direction.

From Fig. 8a it is evident that the modes experience degeneracy at around  $0.4a$  shift. With larger shifts the eigenwavelength difference grows up again forming a periodic dependence of the frequency detuning on shift  $s$ . We also trace the effect of transverse cavity separation  $p$  on the resonant wavelengths and Q-factors for different longitudinal shifts  $s$ . Results are presented in Figs. 8b–f. Almost exact degeneracy is observed at  $s = 0.4a$  for all transverse separations, Fig. 8d. The two principle eigenmodes are resolved in the FDFD numerical simulations with their frequency detuning being much smaller than for the other shifts.

Away from the degeneracy point each mode profile should support the  $180^\circ$  symmetry of the photonic structure around the central point ( $x = y = 0$ ) between two cavities, for example for a magnetic field component it might be written:  $H_z(x; y; z) = m H_z(-x; -y; z)$ , where  $m = +1$  or  $m = -1$  for the two fundamental modes of the couple cavities [40]. These symmetries are visible for mode profiles shown in Fig. 7b and Fig. 9c,d. However, we note that exactly at the degeneracy point, the field profiles of the eigenmodes are defined with the certain ambiguity and must not satisfy the rotational symmetry, since any linear combination of eigenmodes is an eigenmode as well. As shift starts approaching  $0.4a$  we see that field intensity in one of the nanobeams falls down, Fig. 7b for  $s = 0.4a$ . The connection between the modes weakens. As the result the modes settle mostly in one or another nanobeam, Fig. 11b, bottom panel. In more complicated structures, where cavities are tuned by infiltration, similar effects of anticrossing were registered experimentally [35] (there is always some perturbation present, which, strictly speaking, removes the degeneracy, thus in fact both terms — mode degeneracy and anticrossing — can mean the same here). In Fig. 9a the

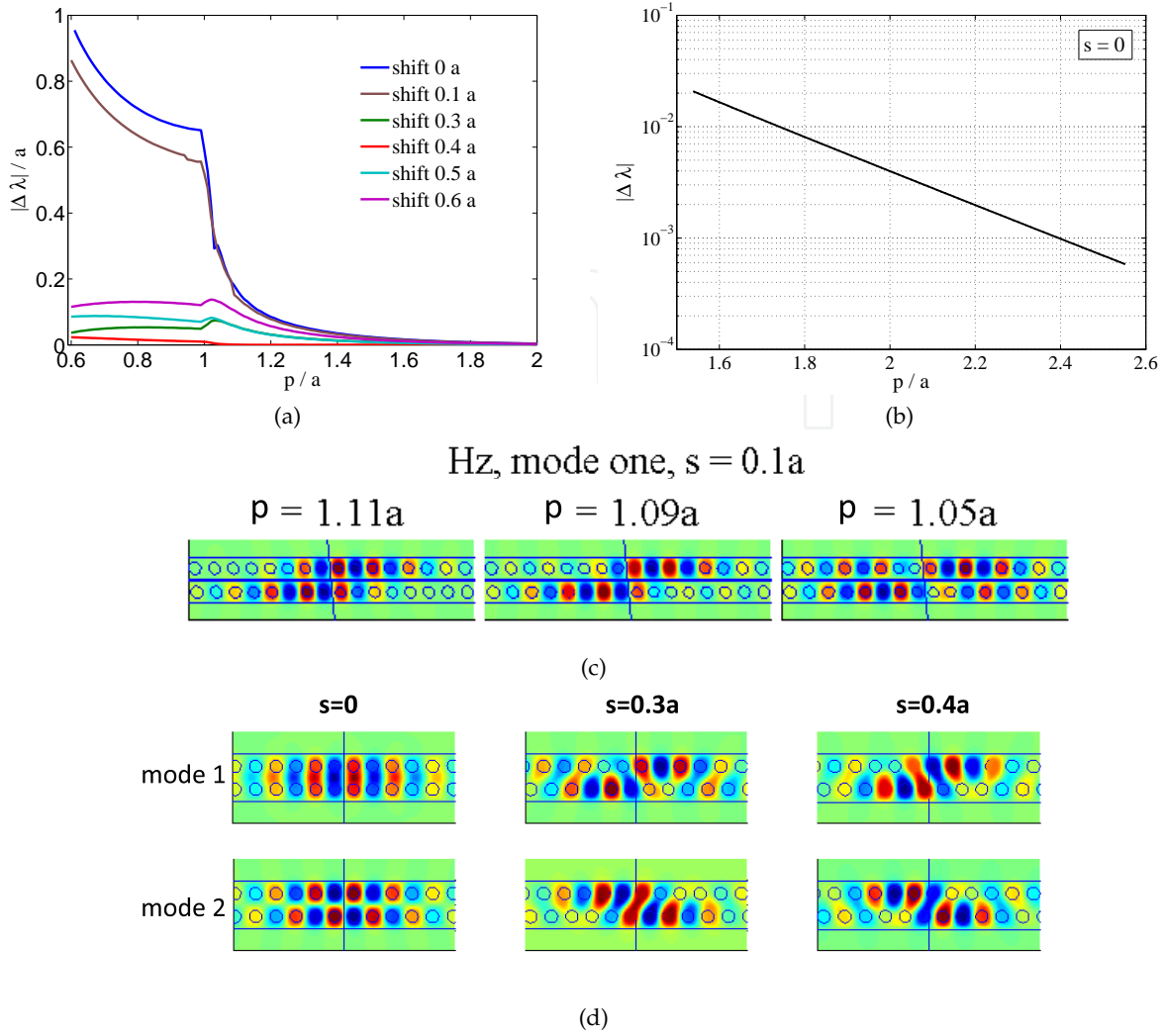


**Figure 9.** (a) Increase of eigenwavelength difference with shortening of transversal separation  $p$  between the nanobeams, different shifts are printed in the legend. (b)  $|\Delta\lambda|$  in logarithmic scale for non-shifted nanobeams. (c) Evolution of magnetic field  $H_z$  in two slightly shifted nanobeams ( $s=0.1a$ ) when closing the air gap between them, i.e. separation  $p$  is reduced from  $1.1a$  to  $1.05a$ . (d)  $H_z$  field distribution in two connected nanobeams with  $p = 0.9a$  at  $s = 0$ ,  $s = 0.3a$  and  $s = 0.4a$  shifts. 2D simulation is made with  $\Delta x = \Delta y \simeq 0.004a$ .  $1a$ -wide  $y$ -buffer (*arctanh* squeezed) is covered by PMLs on half, 3 grid cells come for  $x$ -PMLs.

eigenwavelength difference is plotted showing the highest values for non-shifted resonators and significantly smaller  $|\Delta\lambda|$  for non-zero shifts. Due to the symmetric positioning of  $0.3a$  and  $0.5a$  shift values around the degeneracy point, the wavelength differences given by these shifts are equal to each other for the nanobeams separated by  $p > 1.1a$ . When the nanobeams are far enough transversally and the coupling strength is small,  $|\Delta\lambda|$  depends on  $s$  by the order law seen in Fig. 9b. In Fig. 9b for the illustration purpose the spectral splitting for non-shifted nanobeams is plotted in a logarithmic  $y$ -scale. Other nonzero shifts, except for the degeneracy point, also give similar straight lines in the  $|\Delta\lambda|$ -log scale if separation  $p$  is big enough to correspond to the weak coupling regime.

When the resonators are moved closer so that the interaction between the nanobeams intensifies, all fields, including magnetic one, spread through the air gap. The picture of the mode profiles alters compared to  $p = 1.5a$ , see Fig. 9c,d. Eigenmode fields extend over



the whole cavity even when the hole positions in the upper and lower cavities are effectively shifted in the out-of-phase configuration, i.e.  $s = 0.4a$ . In Fig. 9c the evolution of mode 1 at small shift  $0.1a$  is shown when closing the air gap. Drastic changes occur with the mode 1 profile when the nanobeams are approaching each other: yet very intensive field at  $p = 1.11a$  is pushed out from the cavity center at  $p = 1.05a$ . Thus for nonlinear applications special care should be paid to the extremely thin slots between the nanobeams. Fig. 9d collects field patterns for both modes at different shifts when air-dielectric interfaces are absent and we actually have one cavity consisting of two chirped arrays. Note that although field maps in stitched nanobeams are really complex they are all  $180^\circ$  rotation symmetric relative to the center point. In the degeneracy point  $s = 0.4a$  field is sitting in two nanobeams here. So from the numerical experiment we see that mode picture can look two different ways at the degeneracy: with field concentrated in one of the nanobeams or spreading through both of cavities.

#### 4.1.2. $Q$ and $\lambda$ dependence on the longitudinal shift in 3D

In 3D we consider the same nanobeam design from Fig. 7a and discuss more  $Q$  and  $\lambda$  curves with the rearrangement of the nanobeams. The 3D  $Q$ -factor of a single nanobeam cavity is around  $4 \cdot 10^6$  and the operating wavelength  $\lambda = 3.21a$  for the TE mode, Fig. 6. To achieve fine sampling in 3D problems the symmetry domain reduction is applied where it is possible to satisfy memory requirements. The system of two nanobeam resonators with a longitudinal shift loses plane-reflection symmetry, and the whole domain should be considered so benefits of stretched meshes are fully used here. Discretization in the cavity center is set to  $0.07a - 0.1a$  with a sparser mesh in the rest of the structure (up to 3 times stretching along  $x$ -coordinate). In 3D again  $1a$ -wide buffer layers along  $y$  and  $z$ -direction are covered by PMLs on  $1/3$ , the squeezing function is  $x/(1-x)$ . No air buffer is used along  $x$ -direction, just PMLs comprising 3 grid cells. 3D  $Q$ -factor computations are done on a 48Gb station with the maximum execution time approaching 2 hours per single run. Correct averaging of refractive index at boundaries is an important issue in 3D simulations, where the fine resolution as in the 2D case cannot be achieved. It is important to note that as  $p \rightarrow 1$  a unit Yee cell between two nanobeams might contain two boundaries and then the averaging should be done taking into account both frontiers simultaneously.

Moving nanobeams closer to each other leads to stronger coupling and pronounced increase of the eigenwavelength difference between the doublet of supermodes, see Fig. 10a. At  $p = a$  the system is changed abruptly as the gap between the two nanobeams disappears, so the structure consists now of a single high-dielectric bar with two parallel rows of holes in it. That explains a characteristic peak in the wavelength dependence of the mode eigenfrequency plotted in Fig. 10a. Mode 1 (even) has higher wavelength than mode 2 (odd) for the whole range of separations  $p$  as can be easily seen from a simple perturbation theory [41]. When the gap between nanobeams is closed and the  $y$ -dimension is further reduced, the effective refractive index of the system and hence the eigenwavelengths are also decreased [42]. Remarkably, when varying the separation no significant variation in the  $Q$ -factor is seen. The  $Q$ -factor value is close to  $10^6$  for both even and odd modes, see Fig. 10a.

Now we analyze the effect of longitudinal shift  $s$ . In Fig. 10b the wavelengths and  $Q$ -factors of the fundamental eigenmodes vs. shift  $s$  for separations  $p = 1.2a$  and  $p = 1.5a$  are plotted. As the shift grows from zero, mode detuning is reduced and, independently on separation



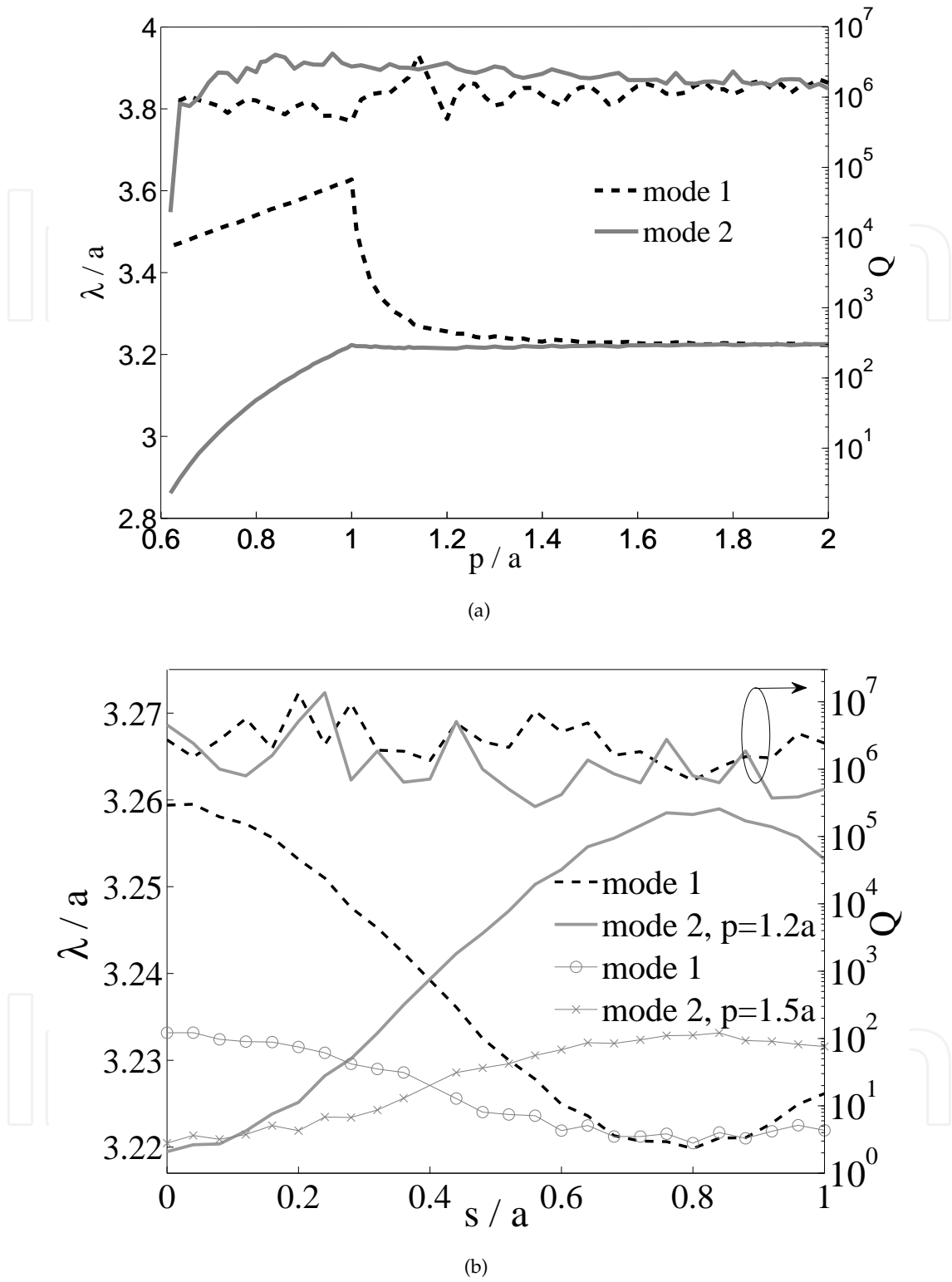


**Figure 10.** Tuning of resonance wavelengths of coupled modes by (a) changing separation between non-shifted ( $s = 0$ ) nanobeams; (b) changing the longitudinal shift  $s$  for two separations ( $p = 1.2a$  and  $p = 1.5a$  as indicated by labels). Right axis shows the 3D  $Q$ -factor values. For 3D simulations  $1a$ -buffers ( $x/(1-x)$  squeezed) along both  $y$  and  $z$ -direction are covered by PMLs on  $1/3$ ,  $x$ -PMLs are 3 cells thick.  $\Delta x = \Delta y = \Delta z$  take values between  $0.07a - 0.1a$  in the center of the nanobeam,  $\Delta x$  is stretched 3 times in the mirror part.

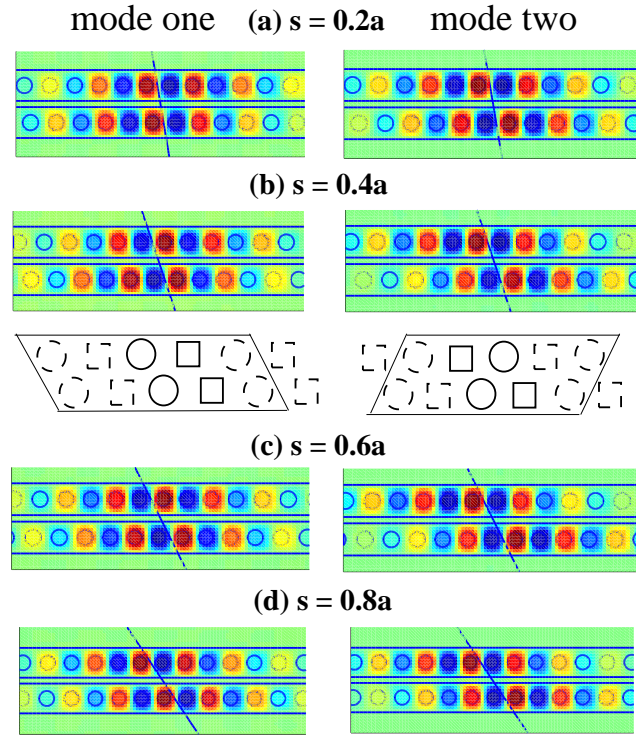


**Figure 11.** Magnetic field  $H_z$  of even and odd modes in coupled nanobeams for  $p = 1.2a$  at different longitudinal shifts.

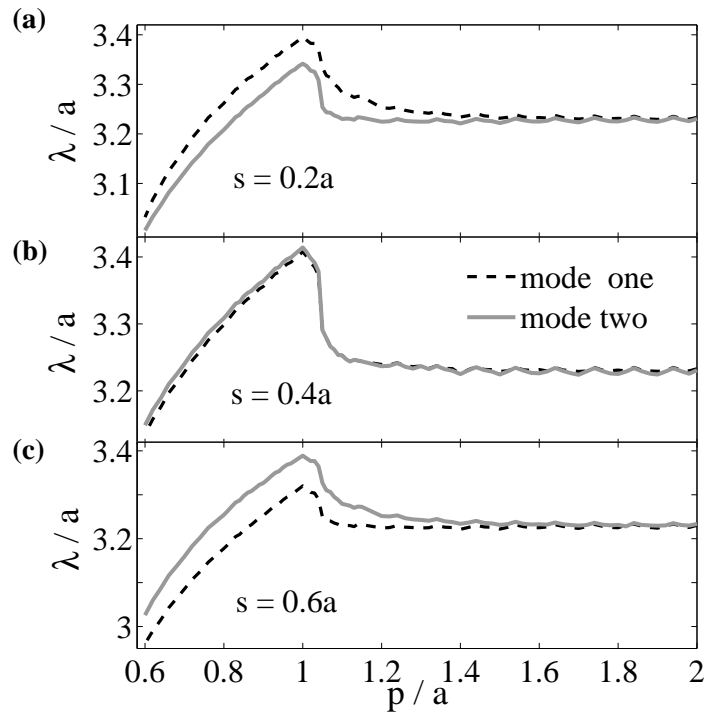


**Figure 12.** Splitting of resonance wavelengths of even and odd modes versus separation  $p$  for (a)  $s = 0.2a$ ; (b)  $s = 0.4a$ ; (c)  $s = 0.6a$ . For 3D simulations  $1a$ -buffers ( $x/(1-x)$  squeezed) along the  $y$  and  $z$ -directions are covered by PMLs on  $1/3$ ,  $x$ -PMLs are 3 cells thick.  $\Delta x = \Delta y = \Delta z = 0.1a$  in the center of the nanobeams,  $\Delta x$  is stretched 3 times in the mirror part.

$p$ , the modes become degenerate at around  $s \simeq 0.4a$ . It is different with resonators with unmodified lattice constant [43], where the degeneracy shift was exactly  $0.5a$  independently on the rod radii variation. Thus, this is primarily variation of the lattice constant that is responsible for the specific value of the degeneracy shift. Note that  $0.4a \simeq 0.5a_6$ , i.e. the shift at the degeneracy point is approximately equal to a half of the average lattice constant in the cavity region.

In Fig. 11b for  $s = 0.4a$  we plot another picture at the degeneracy point compared to Fig. 7b with the magnetic field nodes in one nanobeam opposing field lobes in another. These degenerate modes can be schematically sketched with diagrams in Fig. 11b. Standing wave profiles with slow spatial decay from the center of the cavity towards the periphery allow neglecting low-intensity outer regions and then central parts of the patterns are identical upon reflection, making the occurrence of the degeneracy point (geometrically, the central parts of the defect regions for two modes also satisfy reflection symmetry if chirped hole diameters approximated to be the same in the middle). Had mode profiles less gradual changes in the succession of field minima and maxima along the nanobeams (as shown by bold circles and squares in the diagrams), the formation of the degeneracy would be hardly possible.

For the shifts larger than  $s = 0.4a$  the mode detuning is increased, reaching a maximum at around  $s \simeq 0.8a$  where eigenwavelength difference approaches the same value as at  $s = 0$ . The revival of coupling at  $s \simeq 0.8a$  is again due to the gradually chirped nanobeam design and field profiles extended along the nanobeams. Thus mode detuning depends on the shift almost periodically, and the cavity modes 1 and 2 are adiabatically transformed as the parameter  $s$  is varied from 0 to  $a$ , see Fig. 11d, where it is shown that modes 1 and 2 exchange their parity going from  $s = 0$  to  $s = 0.8$ . Most important, the  $Q$ -factor values remain of the same order of magnitude as for a single cavity.

In Fig. 12 we compare the eigenmodes wavelength dependencies on separation  $p$  for three longitudinal shifts  $s = 0.2a, 0.4a, 0.6a$ . The upper panel shows the reduced spectral detuning of the modes for the intermediate shift  $s = 0.2a$ . The plot in Fig. 12b shows that for non-overlapping nanobeams the modes are almost exactly degenerate at  $s = 0.4a$  for any transverse separation  $p$ . After the degeneracy point, at  $s = 0.6a$  modes 1 and 2 swap their wavelengths.

By comparing Fig. 8 against Figs. 10 and 12 we see that 2D and 3D simulations give essentially similar dependencies for  $\lambda$  and  $Q$  on the longitudinal shift  $s$  and transversal separation  $p$  of the cavities, indicating the possibility to successfully design coupled nanobeam cavity systems in 2D. This is because the physics of side-coupling of dielectric nanobeam cavities is relatively simpler than, for example, the coupling of metallic split-ring resonators where essentially the three-dimensional interplay of magnetic and electric excitations is important.

## 4.2. Three coupled nanobeams

In multiple side-coupled nanobeam cavities modes can also be tuned by longitudinal shift. Degeneration of modes in structures containing many elements amounts to the absence of parasitic coupling between the neighboring units. Instead of increasing the distance between optical components usually employed to minimize the cross-talk, the longitudinal

shift can be proposed to create a dense photonic integrated circuit. Moreover, by taking large enough transversal separation the degeneracy wavelength of coupled nanobeams (up to three resonators in our tests) can be tuned to a single nanobeam resonance wavelength. This potentially allows adjacent waveguiding components, all together, and each separately, to operate at the same wavelength. For example, a compact single-wavelength switch matrix can be created on the basis of a nanobeam-switcher with nonlinearity [20]. Another field of application is building an array of nanobeam cavities to form a quantum optical network where many identical resonators should be placed closely one to another on a chip [44]. Additionally, by controlling the mode coupling it becomes possible to tailor the optical field across an array of multiple nanocavities for applications in particle trapping [27] and optomechanical interactions [18, 19].

#### 4.2.1. Weak coupling regime

We did 2D simulations (letting the nanocavities be infinitely high) to catch basic features of the mode tunability. As usually,  $\Delta x = \Delta y \simeq 0.004a$ ,  $1a$ -wide buffer layers along  $y$ -direction are squeezed with the  $x/(1-x)$  function covered by PMLs on  $1/2$ . No air buffer is used along  $x$ -direction, PMLs comprise 3 grid cells. For three side-coupled nanobeam cavities their relative alignment can be characterized by separations  $p_2, p_3$  and longitudinal shifts  $s_2, s_3$  of the second and third cavities. As an example we consider equally spaced ( $p_2 = p_3 = p$ ) nanobeam cavities, only the middle one being shifted:  $s_2 = s, s_3 = 0$ . Dependence of the modes wavelength detuning (relative to a single cavity) on shift  $s$  is given in Fig. 13a for  $p = 2.3a$ . We observe behavior similar to the case of two nanobeams. Specifically, all three modes become degenerate at  $s \simeq 0.4a$ ; by varying  $p$  we can control the wavelength of the degenerate modes, and it coincides with the wavelength of a single cavity, Fig. 13a. Mode profiles for the non-shifted system ( $s = 0$ ) are shown in Fig. 13b. Note that mode 3 is localized at the outer cavities, so its wavelength is not sensitive to the middle cavity shift as observed in Fig. 13a. There is nice mechanical analogy with modes of three weakly coupled pendulums: in mode 1, all three pendulums are swinging in phase; in mode 2, two outward pendulums move forward while the middle one moves backward; in mode 3, the central pendulum is at rest and two others are moving oppositely.

At the degeneracy point ( $s \simeq 0.4a$ ) the eigenmode profiles are primarily localized at individual cavities, see Fig. 13c. In Fig. 13c the mode profiles at  $s = 0.41a$  reveal complete vanishing of field in neighboring nanobeams whereas for two coupled nanobeams  $s = 0.4a$  shift was more likeable to be called the exact degeneracy shift value. In fact, it is quite difficult to detect the precise value of the degeneracy shift as it requires extremely fine steps in  $s$  and long simulation times; besides, accuracy of computation is also limited by the finite-difference description. However, small deviations from the exact degeneracy do not change field mapping significantly as solutions to Maxwell's equations are all smooth functions.

Wavelength detuning is much less pronounced at  $p = 2.3a$  than at smaller separation. The reason to choose the separation  $p = 2.3a$  is that coupling between the nanobeams is already weak and the energy splitting becomes symmetric relative to the initial energy level as follows from the standard perturbation approach. And the degeneracy wavelength of an array of nanobeams is the same as the isolated nanobeam eigenwavelength (note, that this is not true for the case of strong coupling at  $p = 1.5a$ ).

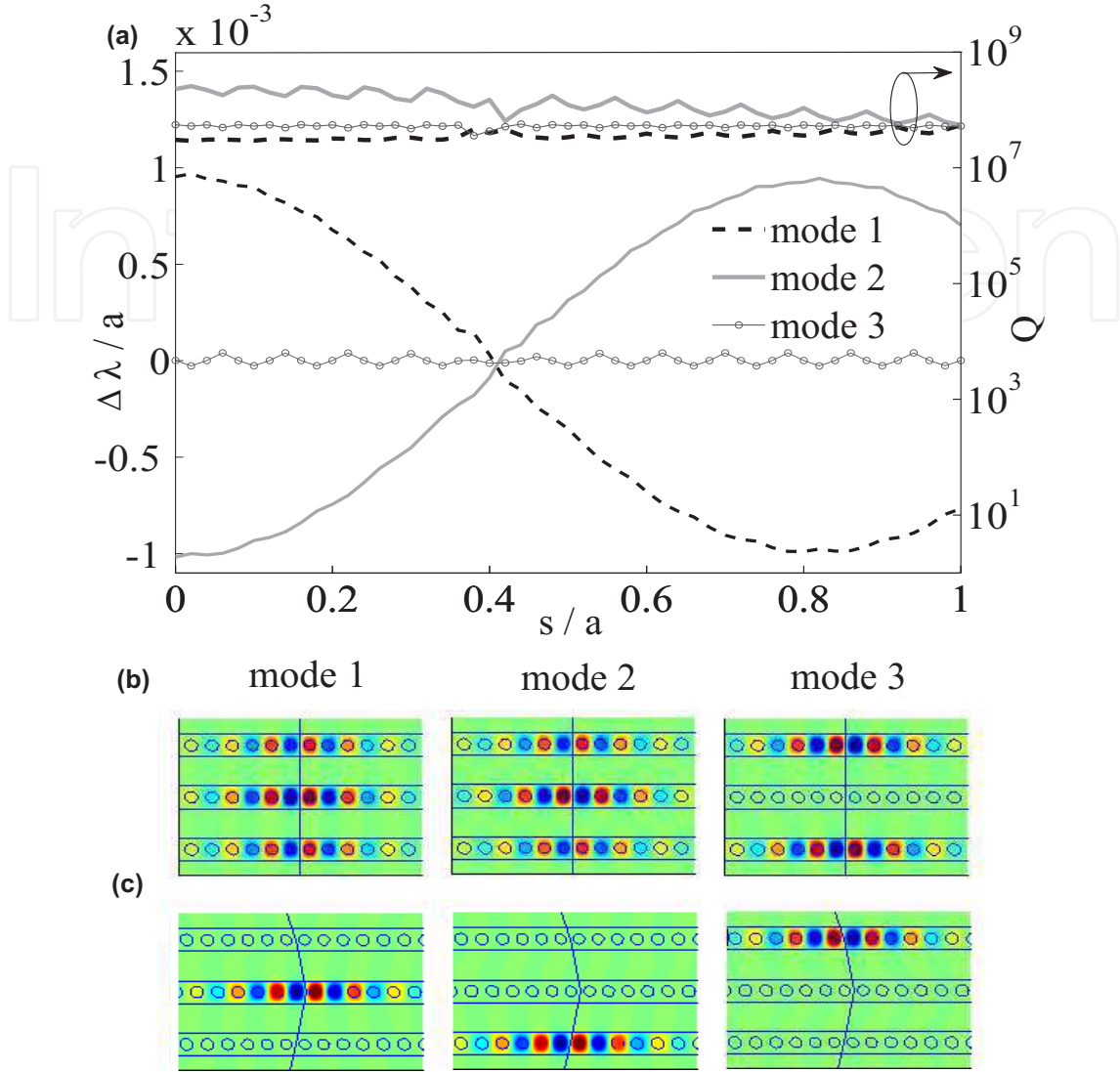


**Figure 13.** Modes in the three side-coupled nanobeam cavities with transversal displacement between the neighboring nanobeams being equal to  $2.3a$ . The middle nanowire is longitudinally shifted, the other two being kept stationary. (a) Spectral detuning of the three modes from the single nanobeam cavity wavelength  $\lambda = 3.9965a$ . Right y-axis—the  $Q$ -factor of the three coupled modes (for an isolated nanobeam cavity,  $Q = 1.5 \cdot 10^8$ ).  $H_z$  profiles for the modes in the three (b) unshifted and shifted (c) by  $0.41a$  nanobeams. For 2D calculation  $\Delta x = \Delta y \simeq 0.004a$ ,  $1a$ -wide  $y$ -buffer is  $x/(1-x)$  squeezed with half of the buffer covered by PMLs,  $x$ -PMLs are 3 grid cells thick.

Although we are in the weak coupling regime, the spectral splitting corresponding to  $p = 2.3a$  is about 0.2%, which for telecom wavelength  $1.5\mu\text{m}$  amounts to 3 nm spread in wavelengths. A comparable shift in the resonance wavelength is induced by inclusion of the nonlinear material in the nanobeam. This allows cavity operation as a switcher totally transmitting or suppressing the signal depending on turning on/off the nonlinearity [20]. Thus 0.2% energy difference for multiple nanobeams placed at  $p = 2.3a$  on a photonic integrated chip introduces parasitic coupling hindering the single-wavelength operation.

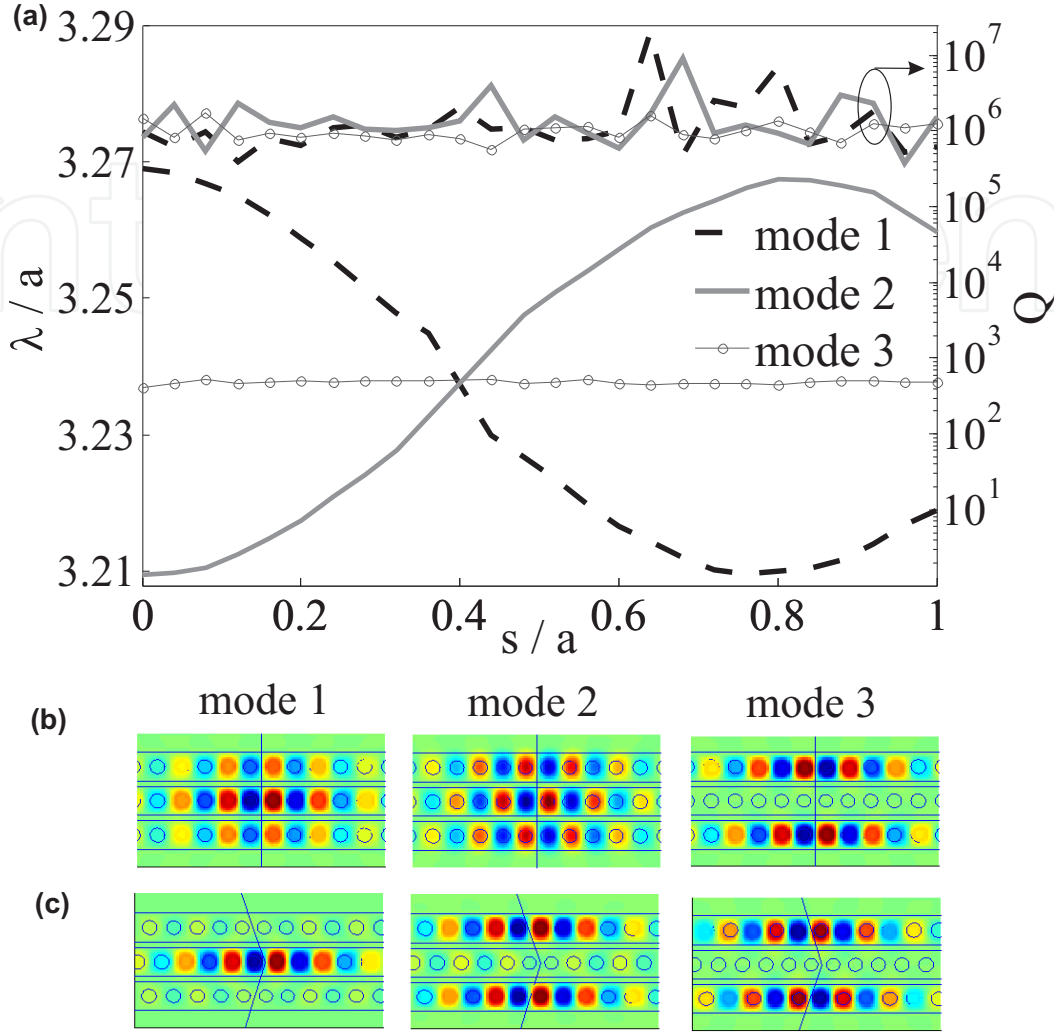


**Figure 14.** Modes in the three side-coupled nanobeam cavities. The middle nanobeam is longitudinally shifted, the other two being kept stationary. Transverse separation between the neighboring nanobeams is  $p = 1.2a$ . (a)  $\lambda$  and  $Q$  of the three modes. (b)  $H_z$  profiles for the modes in the three non-shifted nanobeams. (c)  $H_z$  profiles of the degenerate modes at  $s = 0.4a$ . For 3D simulation  $1a$ -buffer ( $x/(1-x)$  squeezed) along  $y$  and  $z$ -direction is covered by PMLs on  $1/3$ ,  $x$ -PMLs are 3 cells thick.  $\Delta x = \Delta y = \Delta z \simeq 0.09a$  in the center of the nanobeam,  $\Delta x$  is stretched 3 times in the mirror part.

If we further suppose the nonlinear core of a nanobeam cavity, e.g. taking into account the refractive index changing due to nonlinearity, then the degenerate modes in the array of nonlinear cavities can be also tuned to a single resonator wavelength by  $p$  variation. A single-wavelength operating switching array can be build on the basis of such nanobeam cavities that will work equally well for applied single- or multiple-channel excitation. For instance, in the case of the single-cavity nonlinear operation based on 0.03% change in refractive index, the frequency shift due to presence of neighboring ‘passive’ nanobeams is estimated to be around a negligible  $2 \cdot 10^{-4}\%$ .



We have verified that mode degeneracy also occurs in four side-to-side coupled nanobeam cavities. Thus we expect mode degeneracy happening in multiple side-coupled cavities when they have staggered longitudinal shifts, such that neighboring nanowires are shifted longitudinally by  $s \simeq 0.4a$ . We also foresee that the  $Q$ -factor in a multi-cavity structure should remain of the same order of magnitude as that of a single nanocavity.

#### 4.2.2. Strong coupling regime

The strong coupling regime is investigated by doing 3D simulations with symmetry planes enforced through the domain reduction. For three nanobeams dependence of mode detuning on shift  $s$  of the middle nanobeam is given in Fig. 14a for  $p = 1.2a$ . Here three modes become degenerate at  $s \simeq 0.4a$  with wavelength  $\lambda \simeq 3.235a$  bigger than the single 3D nanobeam eigenwavelength  $3.21a$ . 3D  $Q$ -factors for three coupled cavities are found to remain of the same order as the longitudinal shift is varied, see Fig. 14a. Mode profiles for the non-shifted system ( $s = 0$ ) are shown in Fig. 14b. When symmetry planes are enforced the eigenmode profiles at the degeneracy point ( $s \simeq 0.4a$ ) look as in Fig. 14c.

In general, in the degeneracy point we presented the results of our numerical calculations based on the direct solution of Maxwell's equations and without taking linear combinations with data obtained. Our calculations for systems with two and three nanobeams gave two variants of field maps at the degeneracy point:  $180^\circ$  rotational (2 resonators) or reflection (3 resonators) symmetrical pictures with mode profiles exhibiting field localization in individual resonators. Simulations with enforced PEC/PMC perfect conducting planes for the three nanobeams give degenerate modes strictly reflection-symmetrical. However, we can guess that these pictures do not help in understanding physical reality better than do profiles with field localization in individual nanobeams implying complete vanishing of interaction between the cavities. Therefore, the characteristic degeneracy profile with field extinction in one of the cavities that is clearly predominant in all 2D and 3D simulations for all range of separations should be more expectable in the experiments than other linear combinations of the degenerate mode profiles.

## 5. Conclusions

We have suggested and showed numerically that a longitudinal shift in nanobeam cavities significantly alters coupling efficiency between multiple closely packed resonators. Whereas the concept of the longitudinal offset between cavities was previously developed for dielectric rod arrays at microwave frequencies [43] and micro-scale ring resonators at optical wavelengths [32], we have demonstrated here new possibilities for light control at nanoscale. Frequency detuning of coupled modes depends nontrivially on the longitudinal shift of the cavities, in particular, the modes become degenerate for a certain shift, a feature impossible in non-shifted resonators. At this shift of about a half the averaged lattice constant in the defect region, the magnetic field nodes in one nanobeam oppose the field lobes in the other. The degeneracy occurs for a broad range of separations between two or multiple side-coupled cavities. The quality factor of coupled nanobeam cavities stays close to that of a single cavity, indicating good practical prospects for such structures.

## Author details

Aliaksandra M. Ivinskaya<sup>1</sup>, Andrei V. Lavrinenko<sup>2</sup>,  
Dzmitry M. Shyroki<sup>3</sup> and Andrey A. Sukhorukov<sup>4</sup>

1 Department of Micro- and Nanotechnology, Technical University of Denmark, Lyngby, Denmark

2 Department of Photonics Engineering, Technical University of Denmark, Lyngby, Denmark

3 Institute of Optics, Information and Photonics, University Erlangen-Nürnberg, Erlangen, Germany

4 Nonlinear Physics Centre and Centre for Ultra-high bandwidth Devices for Optical Systems (CUDOS), Research School of Physics and Engineering, Australian National University, Canberra, Australia

## References

- [1] K. Hennessy, A. Badolato, M. Winger, D. Gerace, M. Atatüre, S. Gulde, S. Fält, E. L. Hu, and A. Imamoglu. Quantum nature of a strongly coupled single quantum dot-cavity system. *Nature*, 445(7130):896–899, February 2007.
- [2] V. Rao and S. Hughes. Single quantum dot spontaneous emission in a finite-size photonic crystal waveguide: Proposal for an efficient chip single photon gun. *Physical Review Letters*, 99(19):193901, November 2007.
- [3] T. Yoshie, A. Scherer, J. Hendrickson, G. Khitrova, H. M. Gibbs, G. Rupper, C. Ell, O. B. Shchekin, and D. G. Deppe. Vacuum Rabi splitting with a single quantum dot in a photonic crystal nanocavity. *Nature*, 432:9–12, November 2004.
- [4] Y. Zhang, M. W. McCutcheon, I. B. Burgess, and M. Loncar. Ultra-high-Q TE/TM dual-polarized photonic crystal nanocavities. *Optics Letters*, 34(17):2694–2696, September 2009.
- [5] B.-S. Song, S. Noda, T. Asano, and Y. Akahane. Ultra-high-Q photonic double-heterostructure nanocavity. *Nature Materials*, 4(3):207–210, February 2005.
- [6] Z. Zhang and M. Qiu. Small-volume waveguide-section high Q microcavities in 2D photonic crystal slabs. *Optics Express*, 12(17):3988–3995, August 2004.
- [7] O. Painter, J. Vučković, and A. Scherer. Defect modes of a two-dimensional photonic crystal in an optically thin dielectric slab. *Journal of the Optical Society of America B*, 16(2):275–285, February 1999.
- [8] B.-S. Song, S.-W. Jeon, and S. Noda. Symmetrically glass-clad photonic crystal nanocavities with ultrahigh quality factors. *Optics Letters*, 36(1):91–93, January 2011.
- [9] K. J. Vahala. Optical microcavities. *Nature*, 424(6950):839–846, August 2003.
- [10] Y. Tanaka, T. Asano, and S. Noda. Design of photonic crystal nanocavity with Q equal to  $10^9$ . *Journal of Lightwave Technology*, 26(11):1532–1539, June 2008.

- [11] Y. Gong, B. Ellis, G. Shambat, T. Sarmiento, J. S. Harris, and J. Vuckovic. Nanobeam photonic crystal cavity quantum dot laser. *Optics Express*, 18(9):8781–8789, April 2010.
- [12] P. B. Deotare, M. W. McCutcheon, I. W. Frank, M. Khan, and M. Loncar. High quality factor photonic crystal nanobeam cavities. *Applied Physics Letters*, 94:121106–3, 2009.
- [13] Ph. Lalanne C. Sauvan, G. Lecamp and J. P. Hugonin. Modal-reflectivity enhancement by geometry tuning in photonic crystal microcavities. *Optics Express*, 13:245–255, 2005.
- [14] P. B. Deotare, M. W. McCutcheon, I. W. Frank, M. Khan, and M. Loncar. Coupled photonic crystal nanobeam cavities. *Applied Physics Letters*, 95(3):031102, 2009.
- [15] N.-V.-Q. Tran, S. Combri  , and A. De Rossi. Directive emission from high-Q photonic crystal cavities through band folding. *Physical Review B*, 79(4):041101, January 2009.
- [16] S.-H. Kim, S.-K. Kim, and Y.-H. Lee. Vertical beaming of wavelength-scale photonic crystal resonators. *Physical Review B*, 73(23):235117, June 2006.
- [17] Y. Gong and J. Vuckovic. Photonic crystal cavities in silicon dioxide. *Applied Physics Letters*, 96(3):031107, 2010.
- [18] M. Eichenfield, R. Camacho, J. Chan, K. J. Vahala, and O. Painter. A picogram- and nanometre-scale photonic-crystal optomechanical cavity. *Nature*, 459(7246):550–555, May 2009.
- [19] Q. Lin, J. Rosenberg, D. Chang, R. Camacho, M. Eichenfield, and K. J. Vahala. Nano-optomechanical structures. *Nature Photonics*, 4:236–242, April 2010.
- [20] M. Belotti, M. Galli, D. Gerace, L. C. Andreani, G. Guizzetti, A. R. Md Zain, N. P. Johnson, M. Sorel, and R. M. De La Rue. All-optical switching in silicon-on-insulator photonic wire nano-cavities. *Optics Express*, 18(2):1450–1461, January 2010.
- [21] A. Yariv, Y. Xu, R. K. Lee, and A. Scherer. Coupled-resonator optical waveguide: a proposal and analysis. *Optics Letters*, 24(11):711–3, June 1999.
- [22] D. Gerace, H. E. T  reci, A. Imamoglu, V. Giovannetti, and R. Fazio. The quantum-optical Josephson interferometer. *Nature Physics*, 5(4):281–284, March 2009.
- [23] D. G. Angelakis, L. Dai, and L. C. Kwek. Coherent control of long-distance steady-state entanglement in lossy resonator arrays. *Europhysics Letters*, 91(1):10003, July 2010.
- [24] K. A. Atlasov, M. Felici, K. F. Karlsson, P. Gallo, A. Rudra, B. Dwir, and E. Kapon. 1D photonic band formation and photon localization in finite-size photonic-crystal waveguides. *Optics Express*, 18(1):117–22, January 2010.
- [25] K. Foubert, L. Lalouat, B. Cluzel, E. Picard, D. Peyrade, F. de Fornel, and E. Hadji. An air-slotted nanoresonator relying on coupled high Q small V Fabry-Perot nanocavities. *Applied Physics Letters*, 94(25):251111, 2009.

- [26] B. Cluzel, K. Foubert, L. Lalouat, J. Dellinger, D. Peyrade, E. Picard, E. Hadji, and F. de Fornel. Addressable subwavelength grids of confined light in a multislotting nanoresonator. *Applied Physics Letters*, 98(8):081101, 2011.
- [27] S. Mandal, X. Serey, and D. Erickson. Nanomanipulation using silicon photonic crystal resonators. *Nano Letters*, 10(1):99–104, January 2010.
- [28] F. Intonti, S. Vignolini, F. Riboli, M. Zani, D. S. Wiersma, L. Balet, L. H. Li, M. Francardi, A. Gerardino, A. Fiore, and M. Gurioli. Tuning of photonic crystal cavities by controlled removal of locally infiltrated water. *Applied Physics Letters*, 95(17):173112, 2009.
- [29] H. Altug, D. Englund, and J. Vuckovic. Ultrafast photonic crystal nanocavity laser. *Nature Physics*, 2:484–488, 2006.
- [30] A. E. Miroschnichenko, S. Flach, and Y. S. Kivshar. Fano resonances in nanoscale structures. *Reviews of Modern Physics*, 82:2257–2298, 2010.
- [31] T. Baba. Slow light in photonic crystals. *Nature Photonics*, 2(8):465–473, August 2008.
- [32] J. D. Domenech, P. Munoz, and J. Capmany. Transmission and group-delay characterization of coupled resonator optical waveguides apodized through the longitudinal offset technique. *Optics Letters*, 36(2):136–8, January 2011.
- [33] S. Mookherjea and A. Yariv. Optical pulse propagation and holographic storage in a coupled-resonator optical waveguide. *Physical Review E*, 64(6):066602, November 2001.
- [34] S. Mookherjea and A. Yariv. Second-harmonic generation with pulses in a coupled-resonator optical waveguide. *Physical Review E*, 65(2):026607, January 2002.
- [35] S. Vignolini, F. Riboli, F. Intonti, D. S. Wiersma, L. Balet, L. H. Li, M. Francardi, A. Gerardino, A. Fiore, and M. Gurioli. Mode hybridization in photonic crystal molecules. *Applied Physics Letters*, 97(6):063101, 2010.
- [36] M. Bayer, T. Gutbrod, J. Reithmaier, A. Forchel, T. Reinecke, P. Knipp, A. Dremin, and V. Kulakovskii. Optical modes in photonic molecules. *Physical Review Letters*, 81(12):2582–2585, September 1998.
- [37] D. M. Shyroki, A. M. Ivinskaya and A. V. Lavrinenko. Modeling of nanophotonic resonators with the finite-difference frequency-domain method. *IEEE Transactions on Antennas and Propagation*, 59:4155–4161, 2011.
- [38] M. Notomi and H. Taniyama. On-demand ultrahigh-Q cavity formation and photon pinning via dynamic waveguide tuning. *Optics Express*, 16(23):18657–66, November 2008.
- [39] D. Chigrin, A. V. Lavrinenko, and C. M. Sotomayor Torres. Nanopillars photonic crystal waveguides. *Optics Express*, 12(4):617–622, 2004.
- [40] M. J. Steel, T. P. White, C. M. de Sterke, R. C. McPhedran, and L. C. Botten. Symmetry and degeneracy in microstructured optical fibers. *Optics Letters*, 26:488–490, 2001.

- [41] L. D. Landau and E. M. Lifshitz. *Quantum Mechanics*. MA Addison Wesley, USA, 1958.
- [42] J. D. Joannopoulos, S. G. Johnson, J. N. Winn, and R. D. Meade. *Photonic Crystals: Molding the Flow of Light*. Princeton Univ. Press, 2001.
- [43] S. Ha, A. A. Sukhorukov, A. V. Lavrinenko, and Y. S. Kivshar. Cavity mode control in side-coupled periodic waveguides: Theory and experiment. *Photonics and Nanostructures - Fundamentals and Applications*, 8(4):310–317, May 2010.
- [44] H. J. Kimble. The quantum internet. *Nature*, 453(7198):1023–30, June 2008.